

# Magnetic field extraction of trap-based electron beams using a high-permeability grid

N. C. Hurst, J. R. Danielson, and C. M. Surko<sup>a)</sup>

*Physics Department, University of California, 9500 Gilman Drive, San Diego, La Jolla, California 92093, USA*

(Received 30 March 2015; accepted 17 June 2015; published online 8 July 2015)

A method to form high quality electrostatically guided lepton beams is explored. Test electron beams are extracted from tailored plasmas confined in a Penning-Malmberg trap. The particles are then extracted from the confining axial magnetic field by passing them through a high magnetic permeability grid with radial tines (a so-called “magnetic spider”). An Einzel lens is used to focus and analyze the beam properties. Numerical simulations are used to model non-adiabatic effects due to the spider, and the predictions are compared with the experimental results. Improvements in beam quality are discussed relative to the use of a hole in a high permeability shield (i.e., in lieu of the spider), and areas for further improvement are described. © 2015 AIP Publishing LLC.  
[\[http://dx.doi.org/10.1063/1.4923460\]](http://dx.doi.org/10.1063/1.4923460)

## I. INTRODUCTION

A key to many recent advances in antimatter science has been the progress made in developing plasma techniques for the trapping, storage, manipulation, and delivery of low-energy antimatter.<sup>1,2</sup> The method of choice for trapping and confinement of antimatter is use of specially designed “Penning-Malmberg” (PM) traps.<sup>3,4</sup> The PM trap uses a uniform magnetic field for radial confinement and an electrostatic potential well for confinement in the magnetic field direction. The trapped particles can be manipulated and then ejected from the trap in a controlled manner to form a beam.<sup>5–7</sup> These techniques have found use in many areas of research, including the trapping of low-energy antihydrogen,<sup>8,9</sup> creation of the positronium molecule (Ps<sub>2</sub>),<sup>10,11</sup> probing defects in materials,<sup>12–15</sup> and biopolymer characterization.<sup>16,17</sup>

Although generating quality beams from a PM trap has been quite successful,<sup>5,6,18</sup> a serious limitation is that the beams reside in a strong magnetic field. This presents a problem for applications that require the particles to be in a magnetic field-free region (i.e., an electrostatic beam).<sup>19–22</sup> For example, electrostatic lenses are used in so-called positron “remoderation” techniques to increase beam brightness, and they have the long-term potential to be used in a positron reaction microscope.<sup>23–25</sup> For these electrostatic techniques to work, the particles need to be extracted from the magnetic field. This turns out to pose a challenge in balancing the tradeoff between a large increase in the beam radius  $\rho_b$  with a similar increase in the mean transverse energy,  $E_{\perp}$ .<sup>26</sup>

Positrons (or electrons) have been successfully extracted from a high magnetic field into a field-free region in previous experiments,<sup>27–32</sup> but all relied on first accelerating the particles to kiloelectronvolt energies. More recently, low-energy ( $\sim 30$  eV) beams from a specially tailored electron plasma in a PM trap, operating at a field of 4.8 T, were

transported to a field-free region and then focused with an electrostatic (Einzel) lens.<sup>26,33</sup> In this case, non-adiabatic beam extraction is accomplished by passing the beam through a hole (5 cm in diameter) in a high-permeability metal shield, such that the magnetic field drops quickly in  $\sim 1$ – $2$  cm from  $B = 1$  mT to  $\ll 0.01$  mT. The magnetic field gradient is large enough for the beam particles to be removed from the field non-adiabatically. However, conservation of canonical angular momentum requires that the beam particles acquire perpendicular momentum impulses as they decouple from the field, and this results in additional beam divergence. In these experiments, the impulse magnitude is proportional to the radial location of the particle from the symmetry axis.<sup>26</sup>

In this paper, a technique is described for reducing the impulse magnitudes by inserting a high-permeability grid of radial spokes (referred to as a “magnetic spider”) into the hole in the shield.<sup>34</sup> The spider is specially designed to have a small, approximately constant tine spacing as a function of distance from the symmetry axis, which acts to minimize the deleterious momentum impulses. Under reasonably optimal, but practical conditions, the perpendicular impulse magnitudes can potentially be reduced by approximately an order of magnitude, as compared with that produced by extraction through a hole in the shield.

The beams described in both the previous work<sup>26</sup> and this work have relatively low currents (e.g.,  $\leq 1$   $\mu$ A), and so, space-charge effects are negligible. In the previous work, beam quality was described by a generalized invariant emittance, which is valid both in the magnetic field and after extraction. Insertion of the spider results in particle loss, violating conservation of the generalized emittance. Consequently, the beams discussed here are characterized only after extraction by the field-free limit of the invariant emittance,  $\epsilon^* \equiv (\rho_b^2 E_{\perp})^{1/2}$ .

This paper is organized as follows: The experimental setup is described in Sec. II. In Sec. III, the different regions of beam propagation are modeled and particle trajectories

<sup>a)</sup>Electronic mail: csurko@physics.ucsd.edu

are calculated. Comparison is made between the momentum impulses predicted for the spider and the hole. Experimental data are presented in Sec. IV for the focusing of electrostatic beams after passing through the spider. In Sec. V, the spider transmission is discussed, including possible sources of observed performance limitations. Comparison of the results presented here with those of previous experiments is discussed in Sec. VI, followed by conclusion in Sec. VII.

## II. DESCRIPTION OF THE EXPERIMENT

Details of the electrostatic beam experiment have been presented previously by Weber,<sup>26</sup> and so, the summary here is brief. A schematic diagram of the experiment is shown in Fig. 1(a). The experiment has three distinct regions. The first region is the high-field PM trap that is centered in the 4.8 T field of a superconducting magnet, where plasma is confined axially by a voltage  $V_c$ , typically 100 V. In the second region, the beam is transported adiabatically from 4.8 T to a final field of 1–10 mT before reaching the spider. This region

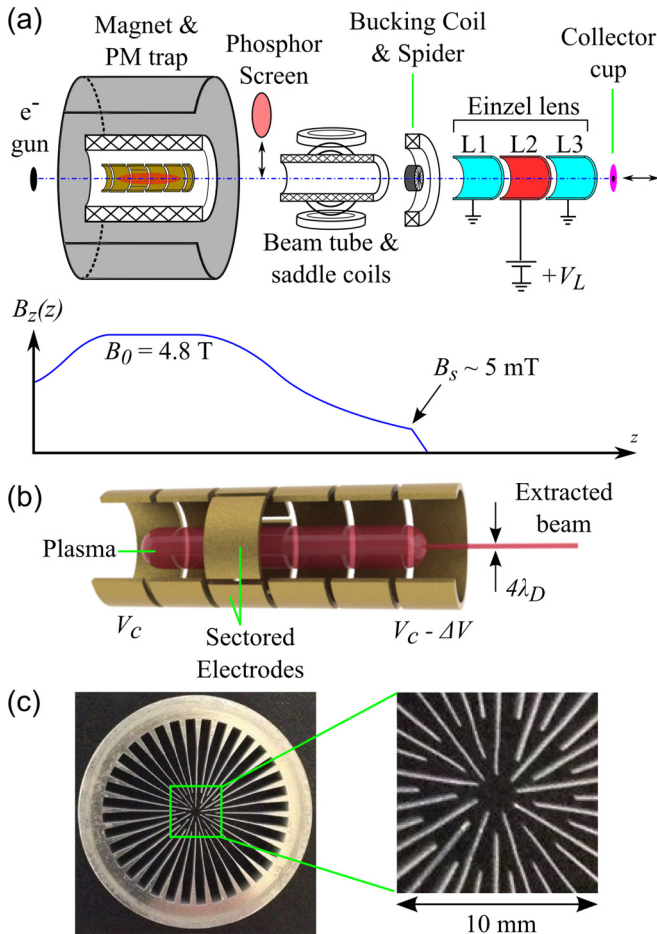


FIG. 1. (a) Schematic diagram of the experiment, with downstream direction left to right, including electron gun, superconducting magnet and PM trap, insertable phosphor screen, beam tube region with saddle coils for beam steering, magnetic spider with bucking coil for adjusting  $B_s$ , Einzel lens consisting of 3 elements, L1 (grounded), L2 (biased to  $+V_L$ ), and L3 (grounded), and translatable collector cup diagnostic. Axial magnetic field is shown schematically. Iron shielding surrounding the electrostatic lens is not shown. (b) Schematic of the high-field Penning-Malmberg trap, including depiction of beam formation; and (c) photograph of the magnetic “spider” with a close-up view on the center.

includes the primary beam tube, two pairs of saddle coils for positioning, and a bucking coil, which is adjusted to define the field at the upstream face of the spider. At the spider, the B-field drops to zero in  $\lesssim 5$  mm, to enter the third, magnetic-field free region. The spider, whose purpose was described earlier, is illustrated in Fig. 1(c). It is made using electron discharge machining from a high-permeability alloy (Carpenter Technology, steel alloy 49), then heated for 4 h at 1200 °C in an oxygen-free hydrogen furnace.<sup>34</sup> The spider was designed with tapered spokes of differing lengths, with the goal of keeping the tine spacing small and simultaneously minimizing beam blockage. In practice, the tine spacing ranges from 0.5–1.4 mm across the range of beam radii studied here.

The third, magnetic-field-free region (i.e., inside of a high magnetic permeability shield), houses a three-element Einzel lens and a charged-particle collector cup with aperture diameter of 2.4 mm. Each lens element (L1, L2, and L3) has an ID of 57 mm and a length of 60 mm. The spider is  $\sim 75$  mm from the front of L1 (165 mm from lens center). The collector assembly (with front plate and cup) is attached to a linear feedthrough, which can traverse  $-20$  mm to  $+40$  mm from the end of L3. Although the techniques described are intended for use with positrons, electrons are used for increased data rate in all the experiments discussed here.

To extract beams, the electrostatic potential on the downstream side of the PM trap is briefly lowered in  $\sim 15$   $\mu$ s to a value  $V_c - \Delta V$ , which is slightly less than the on-axis space-charge potential, and particles near the axis escape (cf. Fig. 1(b)). This technique produces Gaussian radial profiles, of the form  $\sigma_b(r) = \sigma_0 \exp[-(r/\rho_0)^2]$ , where  $\rho_0 \approx 2\lambda_D$ ,  $\lambda_D$  is the plasma Debye length and  $\sigma$  is an areal electron density.<sup>5,6</sup> The areal plasma and beam profiles are imaged using a phosphor screen after the particles are accelerated to  $\sim 5$  keV. The resulting fluorescent light is recorded using a CCD camera.

The range of experimental parameters investigated is summarized in Table I. While trapped, the “rotating wall” (RW) technique is used to control the plasma density,<sup>35,36</sup> and cyclotron radiation cools the electrons to  $\lesssim 0.1$  eV. Use of the RW produces plasma densities in the range  $5 \times 10^8 < n < 1 \times 10^{10} \text{ cm}^{-3}$ , which yields beam radii in the 5 T field in the range  $50 < \rho_0 < 200 \mu\text{m}$ . The mean energy of the beam is set by the on-axis plasma potential. It was typically 35 eV, but could be varied from 15–35 eV. The duration of the beam pulses was typically  $\leq 10 \mu\text{s}$ .

TABLE I. Parameters for the experiments with approximate range of variation and typical values specified. The collector location  $z_c$  is referenced to the downstream end of electrode L3.

Parameter	Symbol	Range	Typical value
Beam radius ( $\mu\text{m}$ )(in 5 T field)	$\rho_0$	50–200	80
Beam radius (mm)(at spider)	$\rho_s$	2–6	2.5
Beam number ( $10^6 e^-$ )	$N_0$	10–100	20
B-field at spider (mT)	$B_s$	2–8	5
Einzel lens voltage (kV)	$V_L$	0–5	3.3
Collector location (mm)	$z_c$	$-20$ to $+40$	$+20$
Beam energy (eV)	$\epsilon_b$	15–35	35

Since the beam parameters are somewhat interdependent, not all parameters could be obtained simultaneously. Thus, the protocol for a given experiment was chosen with the goal of varying only one parameter at a time. Specific details will be discussed on a case-by-case basis in Sec. IV.

After the beam exits the trap, the particles travel adiabatically following field lines through a region of decreasing magnetic field. Conservation of magnetic flux results in an increase in beam radius as the field is decreased

$$\rho_b(z) = \rho_0 \sqrt{B_0/B(z)}, \quad (1)$$

where  $B_0$  is the field in the HF trap. For the experiments presented here, the beam radius at the spider  $\rho_b(z_s)$  is varied from 2 to 6 mm.

Immediately after the spider and before encountering the electric field of the lens, the particles are now in zero magnetic field and travel ballistically. Particle speed is set by the plasma space charge potential in the HF trap. The particles travel at an angle to the axis set by the amount of non-adiabatic impulse (discussed later) they receive upon field extraction.

The electrostatic lens is operated in an acceleration-deceleration mode where the center electrode L2 is biased to a positive voltage  $V_L$  (i.e., for electrons), and L1 and L3 are at ground potential. Once the beam is focused, the  $z$ -integrated intensity is measured using the collector cup.

### III. MODELING BEAM PROPAGATION

Described here are the procedures used to simulate the beam parameters as a result of extraction using the spider that is shown in Fig. 1. These results are compared with those calculated for extraction through a (simple) hole in a high-permeability shield.

#### A. Adiabatic transport

In the guiding-center-drift approximation,<sup>37</sup> the orbital magnetic moment

$$\mu = E_\perp/B, \quad (2)$$

is an adiabatic invariant. This is a good assumption as long as  $\gamma \ll 1$ , where  $\gamma$  is the adiabaticity parameter (considering here a particle travelling in the axial direction)

$$\gamma \equiv \frac{\tau_c}{B} \frac{dB_z}{dt} = \frac{\tau_c v_z}{B} \frac{dB_z}{dz}, \quad (3)$$

with  $\tau_c = 2\pi m/eB$  the cyclotron period, and  $v_z$  the axial velocity of the particle.

The beam radius is given by Eq. (1). Beyond maintaining  $\gamma \ll 1$ , the principal constraint to taking the beam to zero field is the fact that  $\rho_b \rightarrow \infty$  as  $B \rightarrow 0$ .

From conservation of energy, the invariance of  $\mu$ , as  $B$  decreases,  $E_\perp$  must decrease, and thus,  $E_\parallel$  increases by the same amount. In practice,  $E_\perp$  is set by the temperature of the plasma (typically  $T \sim 0.1$  eV), which is much smaller than the parallel energy of the beam (typically  $\sim 35$  eV), and so,

$E_\perp$  can be neglected. Thus, when the beam reaches the end of the adiabatic region, essentially all of the energy is in the parallel degree of freedom. For example, at 5 mT,  $E_\perp \sim 10^{-4}$  eV, and the effective pitch angle is  $v_\perp/v_\parallel \sim 2 \times 10^{-3}$ .

Measurements of  $B(z)$  in the region in front of the spider are shown in Fig. 2(a) for three different bucking coil currents. Shown in Fig. 2(b) are calculations of  $\gamma$  using Eq. (3), for several values of beam energy  $\epsilon_b$ . Typically,  $\gamma \ll 1$ , however, at low  $B$  and high energies,  $\gamma$  approaches unity over an interval  $\sim 5$ – $10$  cm a few centimeters in front of the spider. For completeness,  $\rho_b(z)$  from Eq. (1) is plotted in Fig. 2(c) for the same parameters.

#### B. Non-adiabatic beam extraction

In order to keep the beam from diverging, non-adiabatic extraction is required, namely, a process in which  $\gamma \gg 1$ . The typical experiments reported here use a 35 eV beam energy and a field  $B_s$  at the spider of 50 G, in which case  $\gamma \approx 25$ , which fulfills the nonadiabatic assumption. In this process, often called “fast extraction” from the field, the particles are taken to zero field in a time shorter than the cyclotron period, in which case the particle radius will remain unchanged (i.e.,  $\rho_{bf} = \rho_{bi}$ ). However, the particle will receive an impulse perpendicular to the  $z$  axis due to the Lorentz force arising from the diverging components of the  $B$  field as they terminate on the tines of the spider.

This impulse can be calculated using the change in canonical angular momentum,  $p$ . In the case of a hole in an iron shield (i.e., which obeys cylindrical symmetry),  $p_\theta = mrv_\theta + qr^2B/2$ , where  $q$  is the charge of the particle ( $-e$  for electrons),  $m$  is the electron mass, and the second term is

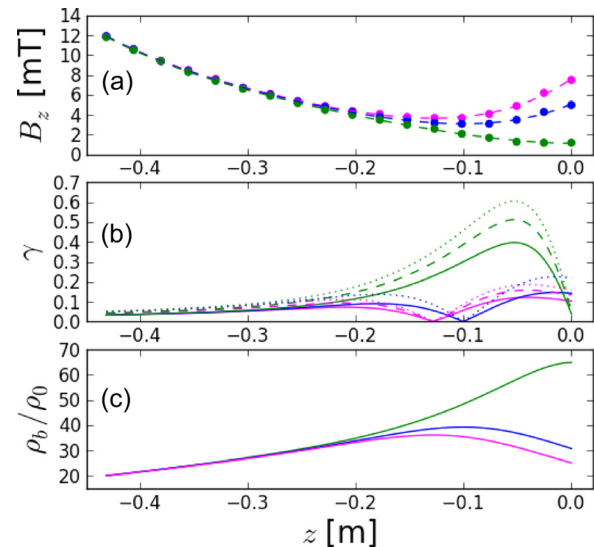


FIG. 2. (a) Axial magnetic field for different values of bucking coil current  $I_{bc} = 1.7$  (green), 3.3 (blue), and 5.8 (magenta) A; (b) the corresponding adiabaticity parameter  $\gamma$  along the beam axis for parallel beam energies  $E_\parallel = 15$  (solid), 25 (dashed), and 35 (dotted) eV; (c) beam radius  $\rho_b$ , normalized to initial radius  $\rho_0$  in the 4.8 T field.  $z = 0$  corresponds to the front face of the magnetic spider, negative  $z$  approaches the magnet and PM trap. In (a), points represent measurements, and the dashed lines represent quartic fits, which are used to calculate  $\gamma$  and  $\rho_b$ . Note that bucking coil can be used to adjust de-coupling field  $B_s$ , and that for typical operating conditions the beam is safely in the adiabatic regime ( $\gamma < 1$ ) throughout the beam tube.

due to the magnetic vector potential. In this case, the magnetic field terminates by converting the axial B-field into a radial field at the hole. Since the terminating magnetic field is in the radial direction, the impulse is in the  $\theta$  direction at finite  $r$ . The impulse velocity experienced by a particle at radius  $r$  is

$$\delta v_\theta = -\frac{e\Delta B r}{2m}, \quad (4)$$

where  $\Delta B$  is the change in the magnetic field.<sup>26</sup> This  $v_\theta$  component has the effect of limiting the ability to focus the beam.<sup>26</sup> The  $r$ -dependence of the impulses implies that keeping the beam small will help to mitigate this effect. However, the size of the beam varies as  $1/\sqrt{B}$ , while the impulses increase proportional to  $B$ . Thus, for a desired (small) beam size, there is a limit to how small the impulses can be made.

The magnetic spider<sup>34</sup> is designed to help circumvent this limitation. Similar designs have been used previously,<sup>28,30,31</sup> but only at larger transport energies than those employed here. The impulses to the particles are dominated by the change in the magnetic vector potential term. In the case of the grid, the spatial scale  $r$  in Eq. (4) is (roughly speaking) replaced by half the grid spacing  $w/2$ . In addition, due to the radial orientation of the spider tines (cf. Fig. 1(c)), the velocity impulses are directed radially, and so, the particles can be better focused using a cylindrical lens. The use of azimuthally oriented tines results in azimuthally directed impulses,<sup>28</sup> and use of parallel slats<sup>30</sup> results in impulses in one Cartesian direction. In both cases, these beams are more difficult to focus as compared with the radial impulses from the spider.

Due to the lack of azimuthal symmetry and the complicated 3D geometry of the spider, it is difficult to calculate the velocity impulses analytically. However, the spider shown in Fig. 1(c) is designed specifically such that the distance between the tines is approximately constant as a function of  $r$ . In this case, the geometry can be approximated using a 2D slab model, as depicted in Fig. 3. Here,  $\theta$  becomes the Cartesian coordinate  $x$ , the spacing between tines is  $w$ , and  $-w/2 \leq x \leq +w/2$ . The changes in velocity are now

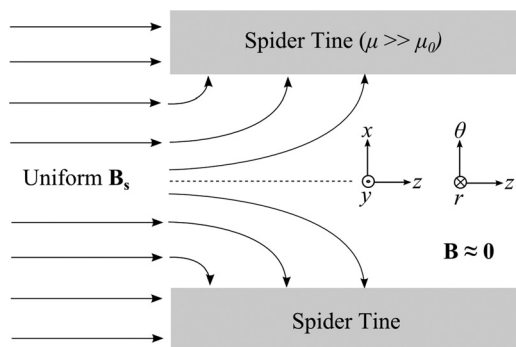


FIG. 3. Schematic diagram of the magnetic field termination, including coordinate axes for both the cylindrical system ( $r, \theta, z$ ) and the slab geometry ( $x, y, z$ ) used to calculate momentum impulses. These impulses are directed radially into and out of the page.

$$\delta v_r = \pm \frac{eB}{m} x. \quad (5)$$

The maximum impulse is received by particles passing close to a spider tine (i.e., near  $x = \pm w/2$ ). Comparing Eqs. (4) and (5), a 1 mm grid spacing reduces the particle impulses by approximately a factor of 10 as compared with the beams studied by Weber.<sup>26</sup> Since the impulses now span both  $\pm r$ , the *average* impulse at any radius will be zero, and the *rms* impulse will be smaller than the maximum by a factor of  $1/\sqrt{3}$ , providing a further reduction in the beam spread.

It is useful to put into perspective the possible utility of the spider for other particle beams (e.g., consisting of protons or other ions). The transverse momentum impulses  $\delta p$  depend on the charge of the particle but not the mass. Therefore, for two particles with equal charge but differing mass, the deflection angle  $\delta v_r/v_z$  will be reduced for the higher mass particle by the square root of the mass ratio. Thus, the impulses are significantly less for ions as compared with electrons or positrons, and so usage of a spider may not be necessary.

### C. Trajectory simulations

The beam from the high-field trap, ejected with parallel energy  $E_{||}$ , is assumed to have a Gaussian radial profile and to be transported adiabatically with beam radius described by Eq. (1). The beam approaches the spider with  $E_\perp \sim 0$ . It is then assumed that the beam is extracted from the field non-adiabatically when it transits the spider. The beam radius is assumed constant, but the particles pick up a distribution of *radial* velocities given by the impulses in Eq. (5). For the experiments described here, the change in the parallel energy is small. In the simulations presented later, the assumptions are that the beam is azimuthally symmetric with the spider transmission fixed at 90% (as demonstrated in Fig. 9). Since the impulses from the spider are only in the radial direction, this assumption should be good as long as the initial beam is cylindrically symmetric.

To model the propagation from the spider to the collector cup, the beam is split into 30 radial locations from  $r=0$  to  $r=3\rho_s$  with a Gaussian radial weighting of the areal density. At each radius, the particles are split into 50 velocities that linearly span the range of impulse velocities  $\pm(eB_s w)/(2m)$ . For each radius and velocity (1500 combinations), a trajectory is calculated by numerically solving the electrostatic equations of motion in two dimensions ( $r, z$ ), using the electrostatic potential expanded to 4th order in displacement from the symmetry axis.<sup>38</sup> This level of approximation is found to be reasonably accurate for trajectories that remain within about half the lens radius (i.e.,  $r < 15$  mm), and it includes effects due to the lowest order chromatic and spherical aberrations.<sup>38</sup> For comparison, the commonly discussed paraxial equations are accurate only to second order and omit all aberrations.

Each trajectory is followed through the lens to the collector. Particles with  $r < 1.2$  mm at the aperture location  $z_c$  are summed to give the expected collector-cup signal  $N_c$ .

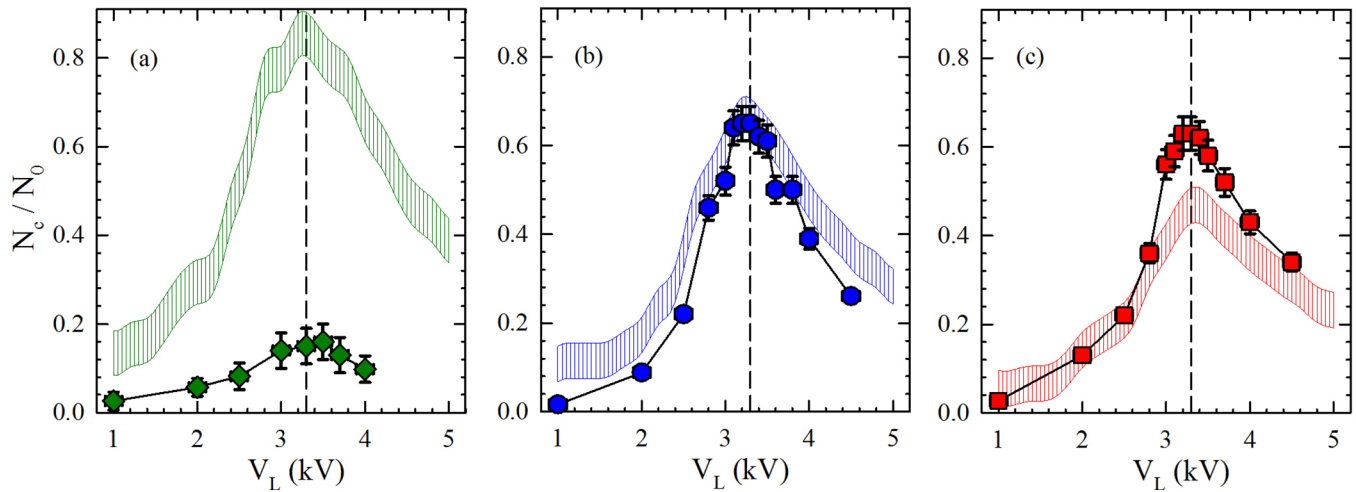


FIG. 4. Normalized number of electrons collected  $N_c/N_0$ , as function of Einzel lens voltage,  $V_L$ , for (a)  $B_s = 20$  G ( $\rho_s = 4$  mm), (b)  $B_s = 50$  G ( $\rho_s = 2.5$  mm), and (c)  $B_s = 80$  G ( $\rho_s = 2$  mm). The mean parallel energy is fixed at  $E_{\parallel} = 35$  eV, and the location of the collector,  $z_c$ , is fixed at 270 mm. The shaded regions correspond to the predictions of the simulations for each  $B_s$  (described in the text). The vertical dashed lines correspond to the focus voltage  $V_f$ .

This signal is calculated for different values of  $V_L$ ,  $\rho_b$ ,  $B_s$ , and  $E_{\parallel}$  for a range of axial collector positions  $z_c$ . Due to uncertainty in the beam radius and magnetic field at the spider, trajectories are calculated with  $\delta v_r$  varied by  $\pm 10\%$  and also with  $\rho_s$  varied by  $\pm 5\%$ . The resulting range of collector signals is shown in the figures below as a shaded region. The presence of the grounded front plate surrounding the collector cup is neglected in the simulations. Previous work has shown that the largest effect of the collector plate on the trajectories is to shift the axial focus point by several millimeters.<sup>26</sup>

#### IV. EXPERIMENTAL RESULTS

The fraction of the beam particles  $N_c/N_0$  that pass through the collector aperture with radius  $r_a = 1.2$  mm is recorded, where  $N_0$  is the total number of particles in the beam pulse. Since the beam radius at the spider varies as  $B_s$  varies, it is not possible to scan all parameters independently. Thus, the radius of the plasma  $\rho_0$  in the high-field trap is adjusted (e.g., by compressing or expanding the plasma with the RW technique), so that the beam parameters at the spider could be held approximately constant.

The lens voltage is varied with the collector position fixed while monitoring  $N_c$ . The “focusing voltage”  $V_f$  is defined as the value of  $V_L$  that maximizes  $N_c$ . Shown in Fig. 4 is  $N_c$  as a function of  $V_L$  for three values of  $B_s$ . As  $B_s$  changes,  $\rho_s$  changes, while the other parameters are held fixed. In this case, the peak signal is  $N_c/N_0 \sim 65\%$  at  $V_L \approx 3.3$  kV, with a fairly broad FWHM  $\approx 1.5$  kV. The shaded region is the range of predictions (including uncertainty) from trajectory simulations described above. The predictions at  $B_s = 5$  and 8 mT agree reasonably well, whereas the data are far below the prediction at  $B_s = 2$  mT.

Data and predictions for  $N_c/N_0$  as a function of beam radius at the spider are shown in Fig. 5 for  $V_L = 3.3$  kV and  $B_s = 50$  G. For these data,  $\rho_0$  is varied using the RW technique in order to vary  $\rho_s$  while leaving  $B_s$  constant. The data follow approximately a  $\rho_s^{-2}$  trend, as shown by the fit in Fig. 5. In

contrast, the simulations show something closer to a linear decrease with increasing beam radius. As a consequence, the predictions are as much as a factor of two higher than the experimental measurements at large  $\rho_s$ . As discussed below, there are several possible sources for this discrepancy, including the possibility of a small tilt of the beam relative to the spider, or other misalignments with the beam axis.

Figure 6 shows the system performance as a function of  $B_s$  for  $\rho_s = 4$  mm. Because adjusting  $B_s$  changes  $\rho_s$ , the beam radius in the 4.8 T field was changed using the RW in order to keep  $\rho_s$  constant. The value of  $\rho_s = 4$  mm is chosen because it is the smallest beam radius accessible for a  $B_s$  variation from 20 to 80 G. Here, the data agree qualitatively with the predictions of the simulations, except at the lowest field; but the magnitudes are lower than the simulation predictions by about 30%. This is similar to the difference shown in Fig. 5 for  $\rho_s = 4$  mm. The general trend over many data sets and corresponding simulations is that the results

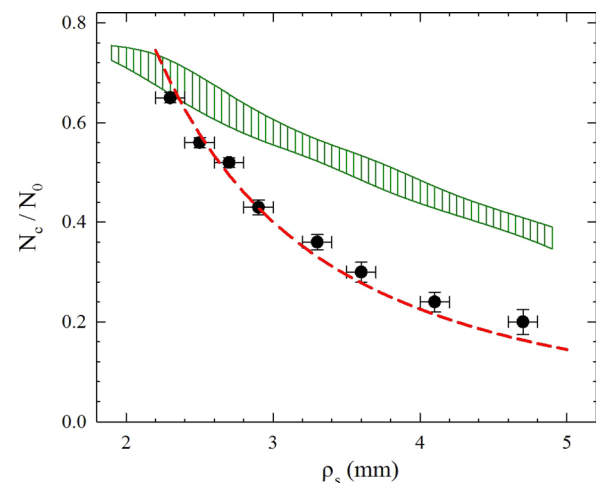


FIG. 5.  $N_c/N_0$  as a function of beam radius at spider,  $\rho_s$ . Fixed parameters are  $B_s = 50$  G,  $V_L = V_f = 3.3$  kV,  $E_{\parallel} = 35$  eV, and  $Z_c = 270$  mm. The shaded region is a prediction from the simulations described in the text, and the dashed curve is a  $\rho_s^{-2}$  fit.

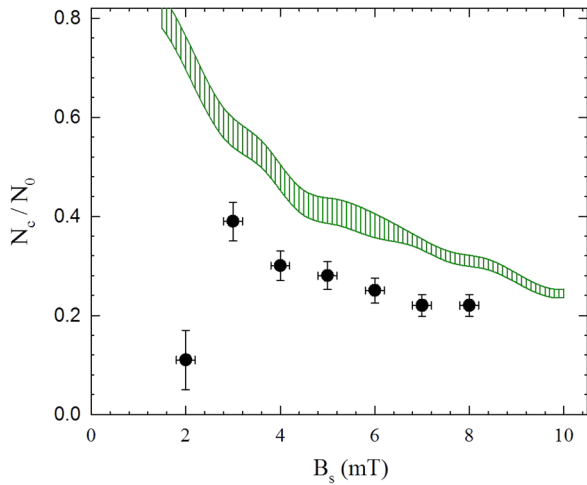


FIG. 6.  $N_c/N_0$  as a function of  $B_s$  for  $\rho_s = 4$  mm,  $V_L = 3.3$  kV,  $E_{\parallel} = 35$  eV, and  $Z_c = 270$  mm. The shaded region is a prediction from the simulations described in the text.

agree best at the smallest values of  $\rho_s$  and at intermediate values of the magnetic field.

The collected beam fraction  $N_c/N_0$  is shown in Fig. 7(a) as a function of the beam energy. A difficulty here is that producing different energy beams requires significantly different plasmas in the 4.8 T PM trap, which makes it difficult to keep

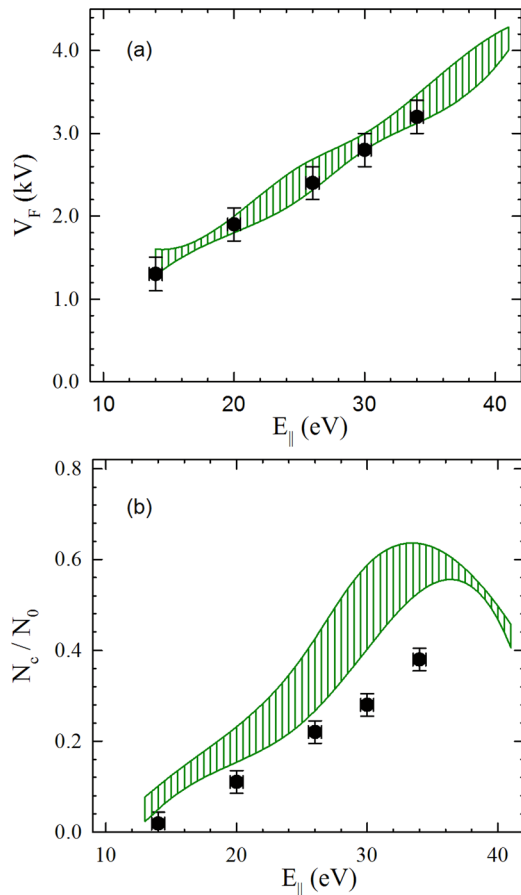


FIG. 7. (a) The lens focus voltage  $V_F$  is shown as a function of  $E_{\parallel}$ . (b)  $N_c/N_0$  at the focus for the data in (a). The parameters are  $B_s = 50$  G and  $\rho_s = 3.2$  mm, and  $Z_c = 270$  mm. The shaded regions are simulation results (see text for details).

the other parameters fixed. For this reason, the total number of beam particles  $N_0$  varied from  $20\text{--}25 \times 10^6$  electrons. Similar to the experiment varying  $B_s$ , in order to keep the beam radius constant as a function of beam energy, a larger beam radius of  $\rho_s \approx 3.2$  mm is required. At each beam energy,  $V_F$  is found by optimizing collector signal. Both the data and simulations show that  $V_F$  increases with  $E_{\parallel}$ , as expected.<sup>39</sup>

Figure 7(b) shows the data for  $N_c/N_0$  as a function of  $E_{\parallel}$  at the optimum focusing voltage. Both the data and simulations show that use of a higher voltage results in a tighter focus, as expected. However, as with the earlier data for larger  $\rho_s$ , the data are about 20%–30% lower than the simulations.

In Fig. 8(a), the lens focal position is measured by optimizing the collector cup position  $z_c$  for different values of  $V_L$ . The data in Fig. 8(b) show the corresponding variation in the magnitude of the collector cup signal  $N_c$ . As expected, both the data and simulations show that, as the collector is moved closer to the lens (smaller  $z_c$ ), a higher lens voltage is required to maximize  $N_c/N_0$ . As shown in Fig. 8(b), once again the data for  $N_c/N_0$  appear to be about 20% lower than the simulation predictions. Additionally, as shown in Fig. 8(a), the observed focusing voltage appears to be about 20% higher than the simulation would predict.

The basic trends in the experiments appear to be described qualitatively by the trajectory simulations that

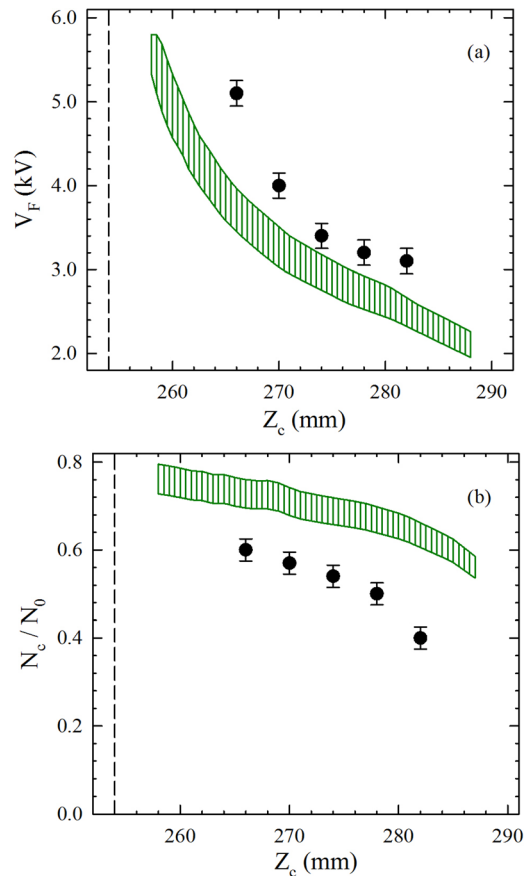


FIG. 8. (a)  $V_L$  for best focus as  $z_c$  is varied. (b)  $N_c/N_0$  at the focus for the data in (a). Fixed parameters are  $B_s = 50$  G,  $\rho_s = 3.2$  mm, and  $E_{\parallel} = 35$  eV. The shaded regions are simulation results (see text for details). Vertical dashed lines represent the end of lens element L3.

assume a simple impulse model for the non-adiabatic extraction. However, the degradation of performance as a function of increasing beam radius (Fig. 5) is worse than the model predicts. Also, the performance is quite poor at the lowest magnetic fields (e.g.,  $B \simeq 20$  G). In Sec. V, a possible explanation for the discrepancy at low  $B_s$  values is discussed.

## V. SPIDER TRANSMISSION

The transmission of the spider can be expressed as  $f_t = 1 - N_s/N_0$ , where  $N_s$  is the number of particles incident upon, and assumed collected by, the tines. Thus, extraction from the magnetic field using the spider introduces an added transmission loss as compared to a hole in a high-permeability plate. The number of transmitted particles  $N_0 f_t$  is measured using the lens electrodes and the collector plate and cup as a single collector. Fig. 9 shows the percentage of the beam transmitted as  $B_s$  is varied. Above 1.5 mT,  $T \approx 90\% \pm 5\%$ . Thus, a constant transmission  $T = 0.9$  is used in the beam focusing simulations for  $B_s > 2$  mT.

However, as shown in Fig. 9, there is an anomalous loss below  $B_s \simeq 2$  mT. One possible explanation for this is that a small misalignment of  $B$  at the spider results in a transverse component of the particle velocity and hence reduced spider transmission, similar to the manner in which venetian blinds block sunlight. Such a transverse field  $B_\perp$  (e.g.,  $B_x$ ) could be caused by magnetic materials in the laboratory and/or misalignment of the magnet and spider axes. The measurements of  $B$  shown in Fig. 2 would not distinguish such a small, yet important  $B_\perp$  component.

Using the geometry of the spider,  $N_s$  can be calculated as

$$N_s = \int_0^\infty dr \int_0^{2\pi} d\theta \sigma_b(r) f_s(r, \theta), \quad (6)$$

where  $f_s$  is the differential fraction of area occupied by the spider at a given location (i.e.,  $\delta A_s / \delta A$ ), and the beam profile is assumed Gaussian, as  $\sigma_b(r) \propto \exp(-(r/\rho_b)^2)$ . For normal beam incidence, the spider is designed such that  $f_s$  is approximately a constant.

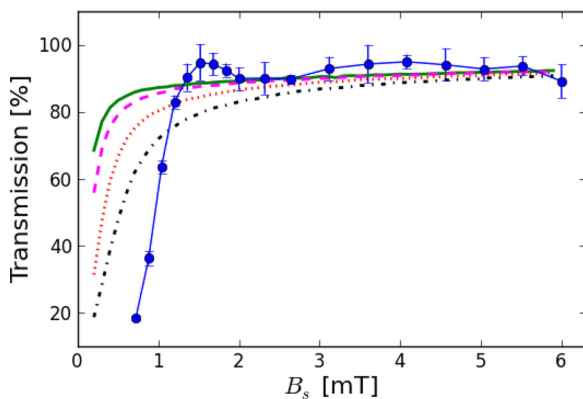


FIG. 9. Experimental (blue circles and solid line) and simulation results for the total spider transmission as a function of  $B_s$ , with  $B_x = 0.01$  (green solid line), 0.02 (magenta dashed line), 0.05 (red dotted line), and 0.1 (black dashed-dotted line) mT (see text for details). Note that for larger  $B_s$ , the value of 90% transmission agrees with that predicted on the basis of the spider geometry.

The geometrical estimate of  $f_{s0} = 0.1$  based on normal beam incidence is consistent with 90% transmission observed for  $B_s \geq 1.5$  mT in Fig. 9. However, if the particles were to follow adiabatically a misaligned field line with a component in a direction  $x$  perpendicular to the  $z$  axis,  $f_s$  would increase as

$$f_s \simeq f_{s0} + \frac{2d}{\pi w} \tan\left(\frac{B_x}{B_z}\right), \quad (7)$$

where  $d \approx 2.5$  mm is the tine thickness in the  $z$ -direction,  $w \approx 1$  mm is the tine spacing, and  $B_z$  is the axial field component. In Eq. (7),  $f_s$  has been averaged over the azimuthal angle with respect to the  $x$  axis. While the tines have a finite thickness  $b$  in the plane perpendicular to  $B$ , the change in spider opacity due to  $b$  when the  $B$  field is tilted is a second order effect and hence is neglected in Eq. (7).

Figure 9 shows the predictions of this model for  $f_t$  as a function of  $B_s$ . For  $B_\perp/B_s \ll 1$ ,  $f_s \approx f_{s0}$ . However, assuming  $B_\perp$  is constant, as  $B_s$  is lowered below about 1–2 mT, the transmission drops precipitously. The qualitative agreement of the simple model and the data, as shown in Fig. 9, indicate that a small misalignment of  $B$  near the spider could give rise to the sharp decrease in  $f_t$  that is observed at low  $B$ .

A small tilt of the beam relative to the normal to the face of the spider is expected to produce other effects. Beyond the problems at low  $B$ , such a tilt would also produce an asymmetric bias (i.e., one Cartesian direction) of the impulses from the spider. This, in turn, could exacerbate lens aberrations and might explain some of the decrease in performance for the larger diameter beams, such as that shown in Fig. 5.

Further improvements in the shielding of the beam and an improved alignment procedure could potentially remedy this difficulty and lead to improved performance. Beam profile measurements immediately downstream of the spider and before the lens would likely be useful in developing a better model for the non-adiabatic impulses at field extraction and also to improve beam alignment.

## VI. COMPARISON WITH PREVIOUS EXPERIMENTS

In Table II, the performance of the arrangement used here is compared with the results of a previous experiment<sup>26</sup> that extracted the beam through a hole in the magnetic shield. In the present experiment, the beam is formed in a 4.8 T field where it has a Gaussian radial profile with  $\rho_0 = 80 \mu\text{m}$  and  $E_{\parallel} \sim 35$  eV. For  $B_s = 5.0$  mT, 65% is collected in an area 0.12 cm in radius at  $V_L = 3.3$  kV. The expected rms  $\delta E_\perp \sim 0.18$  eV. Using  $\rho_s = 0.25$  cm gives an estimated invariant beam emittance of  $\epsilon^* = \approx 0.11$  cm (eV)<sup>1/2</sup>.

In the previous experiment without the spider,<sup>26</sup> the beam started in the same 4.8 T field, but with  $\rho_0 = 65 \mu\text{m}$  and

TABLE II. Focusing performance comparison between using the “spider” vs. the previous experiment using a “hole.”

	$E_{\parallel}$ (eV)	$\delta E_\perp$ (eV)	$B_x$ (mT)	$\rho_b$ (cm)	$V_L$ (kV)	$N_{max}$ (%)	$\epsilon^*$ (cm $\sqrt{\text{eV}}$ )
Hole	30	0.45	1	0.45	5	45	0.3
Spider	35	0.18	5	0.25	3.3	65	0.11

$E_{\parallel} = 30$  eV. Using a 1 mT extraction field at the hole resulted in 45% of the beam focused into an area 1.2 mm in radius at  $V_L = 5$  keV.<sup>26</sup> In this case,  $\delta E_{\perp} \sim 0.45$  eV and  $\rho_b = 0.45$  cm at the hole. This results in  $\epsilon^* \approx 0.3$  cm $\sqrt{\text{eV}}$ . Thus, the invariant emittance without the spider is a factor of three larger, and  $E_{\perp}$  is a factor of 2.5 larger.

With the spider, there is an advantage in trying to work at smaller values of  $B_s$ . This is because, while  $\rho_s \propto (B_s)^{-1/2}$  [i.e., from Eq. (1)], the impulses are independent of  $\rho_s$  but  $\propto B$ , in which case  $\epsilon^* \propto (B_s)^{1/2}$ . Thus, if the spider experiment could be accomplished at  $B_s = 1.0$  mT (assuming the asymmetry could be remedied), the invariant emittance would be reduced by a factor of  $5^{-1/2}$ . Working at larger beam diameters will, however, require additional care in minimizing lens aberrations (e.g., such as use of a larger diameter lens).

Additional routes to improved beams are discussed by Weber.<sup>6</sup> The initial beam radius  $\rho_0$  is proportional to the Debye length. Thus, if one starts with a higher plasma density  $n$  and/or a cryogenically cooled plasma with temperature  $T$ ,  $\rho_0$  is reduced by a factor of  $(T/n)^{1/2}$ . This will reduce  $\rho_s$  and hence lead to a reduced value of  $\epsilon^*$ .

## VII. CONCLUSION

The use of a magnetic grid with radial spokes (the spider) has been shown to reduce the effect of non-adiabatic impulses when transitioning to a magnetic field free region. Comparison to trajectory calculations using a simplified model of the non-adiabatic impulses imparted to the particles as they exit the field shows qualitative agreement with the trends observed. However, reduced performance is observed for beams with larger radii, and also for magnetic fields below about 2.0 mT.

In the field of positron research, the most efficient source of positron beams comes through the use of buffer-gas Penning-Malmberg traps,<sup>40</sup> in which case, the particles necessarily reside in a large magnetic field. For this reason, the techniques described here are expected to be useful in producing higher-brightness positron beams in magnetic-field-free regions.

## ACKNOWLEDGMENTS

We thank Gene Jerzewski for his expert technical assistance. We thank Wolfgang Stoeffl and Darrell Carter for sharing their design of the magnetic spider with us and for helpful conversations. A portion of this work was supported by DOE Grant No. DESC0004661.

<sup>1</sup>C. M. Surko and R. G. Greaves, *Phys. Plasmas* **11**, 2333 (2004).

<sup>2</sup>J. R. Danielson, T. R. Weber, and C. M. Surko, *New Plasma Tools for Antimatter Science* (AIP Press, Melville, NY, 2009), pp. 84–95.

<sup>3</sup>T. J. Murphy and C. M. Surko, *Phys. Rev. A* **46**, 5696 (1992).

<sup>4</sup>C. M. Surko, "Accumulation, storage and manipulation of large numbers of positrons in traps I. - The basics," in *Physics with Many Positrons*, edited by A. P. Mills, Jr. and A. Dupasquier (IOS Press, Amsterdam, 2010), pp. 511–543.

<sup>5</sup>J. R. Danielson, T. R. Weber, and C. M. Surko, *Appl. Phys. Lett.* **90**, 081503 (2007).

<sup>6</sup>T. R. Weber, J. R. Danielson, and C. M. Surko, "Creation of finely focused particle beams from single-component plasmas," *Phys. Plasmas* **15**, 012106 (2008).

<sup>7</sup>M. R. Natisin, N. C. Hurst, J. R. Danielson, and C. M. Surko, "Recent progress in tailoring trap-based positron beams," *AIP Conf. Proc.* **1521**, 154–164 (2013).

<sup>8</sup>C. Amole, M. D. Ashkezari, M. Baquero-Ruiz, W. Bertsche, P. D. Bowe, E. Butler, A. Capra, C. L. Cesar, M. Charlton, A. Deller, P. H. Donnan, S. Eriksson, J. Fajans, T. Friesen, M. C. Fujiwara, D. R. Gill, A. Gutierrez, J. S. Hangst, W. N. Hardy, M. E. Hayden, A. J. Humphries, C. A. Isaac, S. Jonsell, L. Kurchaninov, A. Little, N. Madsen, J. T. K. McKenna, S. Menary, S. C. Napoli, P. Nolan, K. Olchanski, A. Olin, P. Pusa, C. Ø. Rasmussen, F. Robicheaux, E. Sarid, C. R. Shields, D. M. Silveira, S. Stracka, C. So, R. I. Thompson, D. P. van der Werf, and J. S. Wurtele, *Nature* **483**, 439 (2012).

<sup>9</sup>G. Gabrielse, R. Kalra, W. S. Kolthammer, R. McConnell, P. Richerme, D. Grzonka, W. Oelert, T. Seifzick, M. Zielinski, D. W. Fitzakerley, M. C. George, E. A. Hessels, C. H. Storry, M. Weel, A. Müllers, and J. Walz, *Phys. Rev. Lett.* **108**, 113002 (2012).

<sup>10</sup>D. B. Cassidy and A. P. Mills, Jr., *Nature* **449**, 195 (2007).

<sup>11</sup>D. B. Cassidy, T. H. Hisakado, H. W. K. Tom, and A. P. Mills, Jr., *Phys. Rev. Lett.* **108**, 133402 (2012).

<sup>12</sup>R. G. Greaves and C. M. Surko, "Technological applications of trapped positrons," *AIP Conf. Proc.* **498**, 19–28 (1999).

<sup>13</sup>A. David, G. Kögel, P. Sperr, and W. Triftshäuser, *Phys. Rev. Lett.* **87**, 067402 (2001).

<sup>14</sup>P. Egger, W. Sperr, G. Kögel, and H.-J. Gudladt, *J. Phys. Conf. Ser.* **240**, 012164 (2010).

<sup>15</sup>D. W. Gidley, D. Z. Chi, W. D. Wang, and R. S. Vallery, *Ann. Rev. Mater. Sci.* **36**, 49 (2006).

<sup>16</sup>D. Chaudhary, M. R. Went, K. Nakagawa, S. Buckman, and J. P. Sullivan, *Mater. Lett.* **64**, 2635 (2010).

<sup>17</sup>M. Roussanova and M. A. Alam, *J. Phys. Conf. Ser.* **443**, 012044 (2013).

<sup>18</sup>T. R. Weber, J. R. Danielson, and C. M. Surko, *Phys. Plasmas* **16**, 057105 (2009).

<sup>19</sup>M. Charlton and J. W. Humberston, *Positron Physics* (Cambridge University Press, Cambridge, United Kingdom, 2001).

<sup>20</sup>P. G. Coleman, *Positron Beams and their Applications* (World Scientific, Singapore, 2000).

<sup>21</sup>P. J. Schultz and K. G. Lynn, *Rev. Mod. Phys.* **60**, 701 (1988).

<sup>22</sup>C. M. Surko, G. F. Gribakin, and S. J. Buckman, *J. Phys. B: At., Mol. Opt. Phys.* **38**, R57 (2005).

<sup>23</sup>D. S. Slaughter, L. R. Hargreaves, M. A. Stevenson, A. Dorn, J. P. Sullivan, J. C. Lower, S. J. Buckman, and B. Lohmann, *J. Phys: Conf. Ser.* **194**, 072002 (2009).

<sup>24</sup>A. I. Williams, Á. Kövér, D. J. Murtagh, and G. Laricchia, *J. Phys: Conf. Ser.* **199**, 012025 (2010).

<sup>25</sup>T. Pfluger, M. Holzwarth, A. Senftleben, X. Ren, A. Dorn, J. Ullrich, L. R. Hargreaves, B. Lohmann, D. S. Slaughter, J. P. Sullivan, J. C. Lower, and S. J. Buckman, *J. Phys: Conf. Ser.* **262**, 012047 (2011).

<sup>26</sup>T. R. Weber, J. R. Danielson, and C. M. Surko, *Phys. Plasmas* **17**, 123507 (2010).

<sup>27</sup>O. Sueoka, M. Yamazaki, and Y. Ito, *Jpn. J. Appl. Phys., Part 2* **28**, L1663 (1989).

<sup>28</sup>D. Gerola, W. B. Waeber, M. Shi, and S. J. Wang, *Rev. Sci. Instrum.* **66**, 3819 (1995).

<sup>29</sup>R. G. Greaves and C. M. Surko, *Nucl. Instrum. Methods Phys. Res., Sect. B* **192**, 90 (2002).

<sup>30</sup>C. Piochacz *et al.*, *Appl. Surf. Sci.* **255**, 98 (2008).

<sup>31</sup>B. Strasser, C. Hugenschmidt, and K. Schreckenbach, *Radiat. Phys. Chem.* **68**, 627 (2003).

<sup>32</sup>C. Hugenschmidt, J. Mayer, and K. Schreckenbach, *Surf. Sci.* **601**, 2459 (2007).

<sup>33</sup>T. R. Weber, J. R. Danielson, and C. M. Surko, *Rev. Sci. Instrum.* **82**, 016104 (2011).

<sup>34</sup>W. Stoeffl, P. Asoka-Kumar, and R. Howell, *Appl. Surf. Sci.* **149**, 1 (1999).

<sup>35</sup>E. M. Hollmann, F. Anderegg, and C. F. Driscoll, *Phys. Plasmas* **7**, 2776 (2000).

<sup>36</sup>J. R. Danielson and C. M. Surko, *Phys. Plasmas* **13**, 055706 (2006).

<sup>37</sup>F. F. Chen, *Introduction to Plasma Physics and Controlled Fusion, Volume I: Plasma Physics*, 2nd ed. (Springer, New York, 1984).

<sup>38</sup>D. W. O. Heddle, *Electrostatic Lens Systems* (Hilger, 1991).

<sup>39</sup>M. Reiser, *Theory and Design of Charged Particle Beams* (J. Wiley and Sons, New York, 1994).

<sup>40</sup>S. J. Gilbert, C. Kurz, R. G. Greaves, and C. M. Surko, *Appl. Phys. Lett.* **70**, 1944 (1997).